A Local-Area GPS Pseudolite-Based Navigation System for Mars Rovers

Edward A. LeMaster and Stephen M. Rock
Stanford University
Durand Bldg. Rm. 250, Stanford, CA 94305

Abstract

Tasks envisioned for future generation Mars rovers – sample collection, area survey, resource mining, habitat construction, etc. – will require greatly enhanced navigational capabilities over those possessed by the Mars Sojourner rover. Many of these tasks will involve cooperative efforts by multiple rovers and other agents, adding further requirements both for accuracy and commonality between users. This paper presents a new navigation system called a Self-Calibrating Pseudolite Array (SCPA) that can provide centimeter-level, drift-free localization to multiple rovers within a local area by utilizing GPS-based transceivers deployed in a ground-based array. Such a system of localized beacons can replace or augment a system based on orbiting satellite transmitters, and is capable of fully autonomous operations and calibration. This paper describes the basic principles of navigation using an SCPA, focusing on the critical issue of array self-calibration. The new algorithm presented herein – called Quadratic Iterative Least Squares – achieves successful self-calibration 99.80% of the time even under extremely adverse conditions. The paper concludes with a description of the experimental prototype developed to demonstrate these capabilities and presents successful results from field trials which validate both the navigation and self-calibration functions of the SCPA.

1. Introduction

Mars surface exploration presents many challenges for robotic systems. Long communication delays (up to 40 minutes round trip) and limited bandwidth dictate high levels of autonomy. The rovers will be operating in a very uncertain and potentially hostile environment, and in order to perform autonomously they must be able to sense and make sense of the environment around them. This sensing requirement becomes even more critical when multiple rovers or other agents are attempting to cooperate in a common area to do joint tasks such as surveying, resource mining and utilization, or habitat construction.

On Earth, the Global Positioning System (GPS) provides an unlimited number of users with meter-level navigational information on a global scale. By adding a differential reference station, carrier-phase differential GPS (CDGPS) yields centimeter-level, drift free positioning to users operating within a local area. Although a similar system would be of great benefit for Mars exploration, the high launch costs associated with the large number of satellites required precludes this option for the near future. The smaller orbiting positioning and communications network proposed by JPL would be a great asset, but the roughly 10 meter intermittent positioning it would provide is still inadequate for the more precise continuous-time operations envisioned here (Ely et al., 1999).

This paper proposes a new GPS-based local-area positioning system to provide the needed navigation capability. Rather than employing orbiting satellites, small low-power transmitters called pseudolites (short for 'pseudo-satellites') would be distributed on the surface. Multiple users operating in the vicinity of the array could then employ either GPS- or CDGPS-style positioning with respect to these beacons as if they had access to a full GPS satellite constellation and reference station. This concept is illustrated in Figure 1.

In order to use a pseudolite array for navigation, the locations of the broadcasting elements must themselves be known to a corresponding level of accuracy. The precise positions of autonomously distributed pseudolites on the Martian surface will not be known beforehand, however, necessitating the development of methods to survey the locations of the array devices. The proposed system overcomes this difficulty by creating a new type of pseudolite array that is capable of surveying autonomously the locations of the transmitters on the surface after deployment. The resulting system is called a Self-Calibrating Pseudolite Array (SCPA) and utilizes full GPS transceivers instead of separate receivers and pseudolites to accomplish this task.

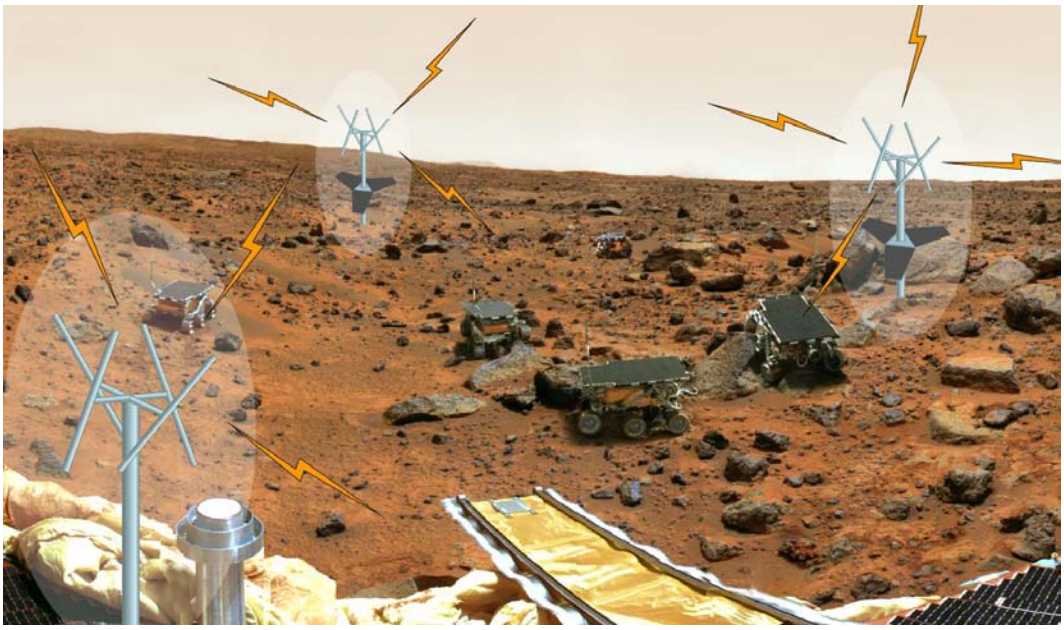

Figure 1: Mars SCPA

Following a brief look at common rover navigation technologies, this paper reviews the basics GPS navigation. It then gives an overview of the new SCPA architecture and then describes the manner in which relative position is determined using an SCPA, both at code-phase (meter) and carrier-phase (centimeter) levels of accuracy. It then discusses the critical issue of array self-calibration – a necessary pre-requisite for SCPA operations – and gives details of the latest self-calibration algorithm. This algorithm, a multiply-seeded iterative process called Quadratic Iterative Least Squares, achieves successful self-calibration 99.80% of the time even under extremely adverse conditions. The final sections of the paper describe the prototype SCPA that has been developed at Stanford to demonstrate these capabilities and then present results from field trials performed at NASA Ames Research Center in June of 2001. These experiments, which utilize the K9 Mars rover research platform, validate both the navigation and self-calibration capabilities of the system.

2. Rover Navigation

Planetary rovers can use a variety of sensors and techniques to help them find their way around an extremely uncertain environment. Common sensors include simple encoders/odometry and inertial units for determining the distance traveled by the rover, and scanning sensors such as laser rangefinders and computer vision systems to detect obstacles. Accelerometers and rate gyros can also be used to detect vehicle attitude, an important addition when traveling over uneven terrain.

Most rover testbeds fuse a number of these different sensors types to enhance both accuracy and robustness. For example, JPL's FIDO Mars rover testbed incorporates wheel odometry, an inertial unit, several cameras in different locations on the chassis, and a sun sensor for heading (Huntsberger et al., 2002; Schenker et al., 2001). NASA Ames's K9 testbed – a FIDO variant – uses odometry, an inertial unit, a mast-mounted stereo camera pair, a scanning laser rangefinder for obstacle avoidance, and a compass for heading, the final instrument not being usable on Mars because of the absence of a global magnetic field (Bresina et al., 2001). Efficient blends of dissimilar types of sensors such as these have been demonstrated to reduce the cumulative position error to a few percent of the distance traveled by the rover (Olson et al., 2001; Chung et al., 2001). Even low sensor drift accumulations such as these, however, can potentially build up unacceptable positioning errors over the course of an extended traverse.

Because of its high accuracy and drift-free properties, many mobile robots use GPS as a position sensor. Those intended for use on other planets, however, only use it as a truth sensor during on-Earth testing because it is presumed to be unavailable on other planets. The research presented here brings the capabilities of GPS back to the navigation system designer, even in the absence of an orbiting constellation of GPS-type satellites.

3. GPS Navigation

In standard GPS navigation, a constellation of orbiting satellites is continually broadcasting a bi-phase shift keyed (BPSK) modulated pseudo-random code on a 1575.42 MHz carrier. Data modulated on top of the code sequence contains information as to the time of broadcast

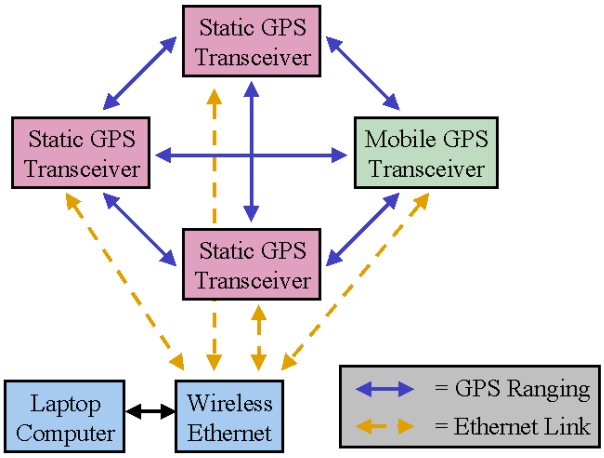

Figure 2: SCPA Architecture

of the signal. User receivers decode that timing information to determine the range (corrupted by the local oscillator error) to each satellite in view. These pseudoranges, when combined with the known satellite locations, allow the user to determine his or her absolute position anywhere on the planet, assuming adequate sky coverage. The high accuracy of the system (currently 3-5 m RMS static accuracy without selective availability (Neilan et al., 2000)) is provided by using regularly updated atomic clocks (~10^{-13} stability) on the satellites and by using a redundant range measurement to cancel out the range errors due to the inexpensive and relatively poor (~10^{-6} stability) oscillator on the receiver.

More-accurate positioning can be done by using differential positioning between the user and a reference receiver at a known, nearby location. This approach exploits the fact that many of the error sources such as ionospheric interference are highly correlated with receiver position, and so appear as common-mode to all users. This technique is especially effective when the receivers are configured to track the carrier instead of the modulated code on the GPS signal. CDGPS can give accuracies on the order of 1 cm, at the expense of adding in an unknown ambiguity in the integer number of wavelengths in the received signals. This ambiguity can be resolved either through a change in system geometry over time or by utilizing multiple frequency signals in a process called wide-laning.

A complete overview of GPS fundamentals can be found in Parkinson et al. (1996).

4. SCPA Navigation

A Self-Calibrating Pseudolite Array duplicates the local-area effects of differential GPS, but without using any orbiting satellites. Unlike conventional GPS satellite or pseudolite systems, which utilize spatially separated broadcast and receive elements, the primary components of an SCPA are full GPS transceivers containing collocated receiving and transmitting devices. Using transceivers as the building blocks of the array yields greater observability of the system states of interest, and is one of the key factors which makes array self-calibration possible. Several of these transceivers are distributed over a local area, and other mobile transceivers within that area effectively triangulate their positions with respect to these stationary devices. At least three stationary transceivers are necessary for unambiguous 2-dimensional positioning.

The general SCPA system architecture is presented in Figure 2. Data from the four transceivers are collected over a wireless network, and are processed at a central base-station computer. Although much of the processing could be distributed, some method of data transmission between the receivers is required for all possible architectures.

4.1 Bidirectional Ranging

Navigation using an SCPA follows the same principle as differential GPS, and can be accomplished at both the code or carrier levels. In order to achieve precise navigation without using atomic clocks, a modification of the standard CDGPS double-difference ranging solution has been developed between the GPS transceivers. The resulting bidirectional inter-transceiver ranging solution involves exchanging ranging signals (corrupted by clock biases) between device pairs.

Equation 1 describes the phase measurement which transceiver *i* makes of an incoming signal *j*. This measurement may be at either code- or carrier-phase accuracy, with the inclusion of the carrier-phase integer ambiguity the only difference in the equation.

$$\phi_i^{(j)} = \left(r_i^{(j)} + \tau_i - \tau^{(i)}\right) + N_i^{(j)} \cdot \lambda + b_i^{(j)} + \nu_i^{(j)} \qquad (1)$$

$\phi_i^{(j)}$ ≡ Measurement of transceiver *j* by transceiver *i*

$r_s^{(i)}$ ≡ Range between transceivers *i* and *j*

τ_i ≡ Clock bias in receiver *i*

$\tau^{(j)}$ ≡ Clock bias in pseudolite *j*

$N_i^{(j)}$ ≡ Carrier-phase integer between transceivers *i* and *j*

λ ≡ Carrier wavelength (19.0 cm)

$b_i^{(j)}$ ≡ Line biases in the measurement between transceivers *i* and *j*

$\nu_i^{(j)}$ ≡ Random noise in the measurement between transceivers *i* and *j*

Transceiver *i* then compares this measurement of transceiver *j* with a measurement of its own broadcast signal. The single-difference measurement formed by the subtraction of these two signals eliminates receiver *i*'s clock bias, and results in Equation 2.

$$\begin{aligned}\Delta\phi_i^{(j,i)} &= \phi_i^{(j)} - \phi_i^{(i)} \\ &= r_i^{(j)} + (\tau^{(j)} - \tau^{(i)}) + (N_i^{(j)} - N_i^{(i)})\lambda \\ &\quad + (b_i^{(j)} - b_i^{(i)}) + (\nu_i^{(j)} - \nu_i^{(i)})\end{aligned} \quad (2)$$

Note that for a general transceiver architecture with unsynchronized oscillators there will still be a clock bias from pseudolite *i*, and the line bias from pseudolite *i* to receiver *i* will not be zero.

The single-difference measurement above is then combined with a similar set of measurements from transceiver *j*, yielding the fundamental bidirectional ranging equation below.

$$\begin{aligned}\nabla\Delta\phi_{i,j} &= \Delta\phi_i^{(j,i)} - \Delta\phi_j^{(j,i)} \\ &= 2\cdot r_i^{\,j} + \nabla\Delta N_{i,j}\cdot\lambda + \nabla\Delta b_{i,j} + \nabla\Delta\nu_{i,j}\end{aligned} \quad (3)$$

$$\nabla\Delta N_{i,j} \equiv N_i^{(j)} - N_i^{(i)} + N_j^{(i)} - N_j^{(j)}$$

$$\nabla\Delta b_{i,j} \equiv b_i^{(j)} - b_i^{(i)} + b_j^{(i)} - b_j^{(j)}$$

$$\nabla\Delta\nu_{i,j} \equiv \nu_i^{(j)} - \nu_i^{(i)} + \nu_j^{(i)} - \nu_j^{(j)}$$

The advantage of this process over conventional double-difference solutions involving separated transmit and receive elements is that it yields the actual range between the pair of transceivers as a direct observable, although this may be corrupted slightly by the unknown differential line biases (generally assumed small). This turns the positioning problem into one of simple trigonometry. As is apparent from Equation 3, however, bidirectional ranging at the carrier level still suffers from the integer ambiguity present in standard CDGPS. A special self-calibration process is used to resolve these integer ambiguities.

4.2 Self-Calibration

Array self-calibration to determine the array geometry and the location of the rover (and hence the carrier-phase integers) follows a multi-step process, as is illustrated in Figure 3. Following deployment, relative navigation is accomplished by combining the range measurements between transceiver pairs, either using triangulation or standard non-linear optimization techniques. Code-level positioning is available instantaneously, allowing a rough (2-4 meter) navigation capability to all users within the array. It is also available with range measurements to as few as two static transceivers, allowing operation within sparse arrays. This 2-4 meter precision can be improved by either short- or long-period averaging. Although uncalibrated line biases and multipath can degrade the accuracy to several meters, code-based ranging is sufficient for many tasks such as general navigation between points and collision avoidance. It may be insufficient, however, for more complex or repetitive tasks such as cooperative manipulation or construction. In these cases, it is necessary to have the centimeter-level accuracy associated with carrier-phase operations.

Achieving carrier-phase positioning is only possible after an additional calibration step is used to resolve the associated integer ambiguities. The prototype system calibrates itself by using the relative motion of a transceiver-bearing rover to alter the array geometry over time. During this motion the unknown integers remain constant. A batch process collects range data during the course of this maneuver, and is subsequently able to determine both the integers and the actual positions of the static transceivers to centimeter-level accuracy via a non-linear iterative optimization process. At least three range measurements from the rover to the static transceivers must be available, and rover motion must be considerable – but not unreasonably so – for successful convergence. For example, a circumnavigation of the array by the rover is sufficient. Note that the rover does not have to drive a tightly defined trajectory in order to calibrate the array, because the algorithm backs out the actual rover trajectory as part of its solution. This calibration process can also be used to remove unknown line biases from the code-range solution.

5. Self-Calibration Algorithms

5.1 Overview

During the course of the self-calibration process, the entire state of the system is determined from the range data between the mobile and stationary transceivers. The states of interest are the locations of the stationary transceivers, the location of the mobile transceiver at any given time, and the constant carrier-phase integer biases in the range measurements. This process therefore falls into the class of applications known as Simultaneous Localization and Mapping (SLAM). SLAM techniques have been applied to many different robotic applications. Some interesting examples include localization of

vehicles in forested areas (Guivant et al., 2000) and underwater (Williams et al., 2000).

Typical SLAM methods invoke a number of sensors to provide high observability of the states of interest – although they will generally not be fully observable at any given instant of time – and then use non-linear filters such as the Extended Kalman Filter (EKF) to provide an estimate from the sensor data. The current experimental system, on the other hand, uses a very limited set of sensor data: the range measurements between the transceivers, which may be biased by amounts as large as the true ranges themselves. This is done both to reduce system complexity and cost, and to show the ultimate capabilities of the SCPA in the absence of any external sensors. Because it is extremely difficult to build an EKF that converges under such large nonlinearities, the self-calibration computation is done as a batch process on a time-series of collected data. This batch methodology is extremely effective at determining the precise array configuration. An operational SCPA on the surface of Mars would likely incorporate many sensors together with the GPS system, use an EKF to provide a rough state estimate during the self-calibration trajectory, and then use the batch process described here to eliminate the residual errors once the trajectory is completed.

This research has examined the performance of four different batch algorithms for the carrier-phase self-calibration of pseudolite transceiver arrays. The first is standard linear iterative least squares (ILS). The second is a new custom variant called quadratic ILS (QILS) which retains 2nd-order terms in the Taylor series expansion in order to better model the array geometry. Finally, both the ILS and QILS are employed in a multiply-seeded approach which greatly enhances their raw performance. This section examines each of these four algorithms, and shows details of their effectiveness for a variety of SCPA configurations.

5.2 Linear Algorithm

The positions of receivers using conventional satellite-based GPS – both with conventional and differential techniques – is generally determined using linear algorithms. This is possible because the only major unknown system states are associated with the receiver itself, and because the great distance to the satellites makes the system largely unaffected by errors in the initial system estimate. In contrast, determination of the locations of the transceivers in an SCPA is a much more difficult task. None of the system states are known beforehand to high accuracy, and the near-field geometry makes the solution very sensitive to small changes in device location. As a consequence, completely linear algorithms are of limited effectiveness in the SCPA calibration process.

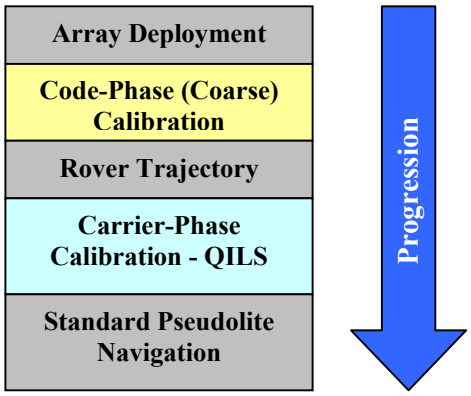

Figure 3: Self-Calibration Process

In situations where the initial array estimates are reasonably close to the true system states, pseudo-linear methods may still be useful. The most straightforward extension of standard GPS solution techniques to the challenges presented by the SCPA is iterative least squares. This is also the technique used in the previous work on SCPAs (LeMaster and Rock, 1999), and therefore makes a useful baseline with which to compare the latest generation of self-calibration algorithms.

During ILS the array geometry is linearized around the initial estimate of the system state generated by code-phase ranging, and the predicted range values are compared to the actual bidirectional range measurements. Differences from this comparison are then applied to the linear system gradient, which moves the state estimate to a new location. The process is then repeated until the solution converges.

Although the baseline ILS algorithm is able to successfully self-calibrate the array when the initial estimation errors are small, it provides inadequate performance when those estimation errors become larger. Such conditions could potentially occur with an SCPA deployed on the Martian surface. This shortcoming of the traditional ILS techniques is demonstrated in Section 5.5.

5.3 Quadratic Algorithm

The need for more effective self-calibration algorithms for use in situations with large initial error estimates has led to a re-examination of the standard linear ILS techniques. The most important factor in the failure of the self-calibration attempts is that the linearization about the estimated states ceases to become an accurate representation of the true array geometry when those estimates are poor. It is therefore highly desirable to have a solution algorithm that retains some of these non-linear characteristics. The search for such an algorithm has led to the development of a solution technique called

Quadratic Iterated Least Squares (QILS). Although this is still not a closed-form solution and does not guarantee successful convergence, the non-linear terms included in the iteration process yield a significant increase in self-calibration effectiveness, especially in the presence of large biases.

This section presents the derivation of the QILS algorithm. Some of the notation used throughout the discussion appears below.

$\mathbf{p}^{(i)}$	$\equiv$	Position of stationary transceiver *i*
$\mathbf{p}_{m,s}$	$\equiv$	Position of mobile transceiver at sample point *s*
$r_s^{(i)}$	$\equiv$	Range between transceiver *i* and the mobile transceiver at point *s*
$b_m^{(i)}$	$\equiv$	Bias between transceiver *i* and the mobile transceiver

Derivation of the Quadratic Iterative Least Squares algorithm follows the same progression as for standard iterative least squares, with exception that 2nd-order perturbations around the estimated array configuration are included instead of merely the linear gradient. The relation for the perturbation in a single range measurement may be written as

$$\delta r_s^{(i)} \cong \nabla f\left(b_m^{(i)}, \hat{\mathbf{p}}^{(i)}, \hat{\mathbf{p}}_{m,s}\right) + \nabla^2 f\left(b_m^{(i)}, \hat{\mathbf{p}}^{(i)}, \hat{\mathbf{p}}_{m,s}\right) \quad (4)$$

where the linear term is

$$\nabla f\left(b_m^{(i)}, \hat{\mathbf{p}}^{(i)}, \hat{\mathbf{p}}_{m,s}\right) = \begin{bmatrix} 1 & \dfrac{\partial \hat{r}_s^{(i)}}{\partial \mathbf{p}^{(i)}} & \dfrac{\partial \hat{r}_s^{(i)}}{\partial \hat{\mathbf{p}}_{m,s}} \end{bmatrix} \begin{bmatrix} \delta b_m^{(i)} \\ \delta \hat{\mathbf{p}}^{(i)} \\ \delta \hat{\mathbf{p}}_{m,s} \end{bmatrix} \quad (5)$$

and the quadratic term is

$$\begin{aligned} &\nabla^2 f\left(b_m^{(i)}, \hat{\mathbf{p}}^{(i)}, \hat{\mathbf{p}}_{m,s}\right) \\ &= \frac{1}{2}\begin{bmatrix} \left[\delta \hat{\mathbf{p}}^{(i)}\right]^T & \left[\delta \hat{\mathbf{p}}_{m,s}\right]^T \end{bmatrix} \begin{bmatrix} \dfrac{\partial^2 \hat{r}_s^{(i)}}{\left[\partial \hat{\mathbf{p}}^{(i)}\right]^2} & \dfrac{\partial^2 \hat{r}_s^{(i)}}{\partial \hat{\mathbf{p}}^{(i)} \partial \hat{\mathbf{p}}_{m,s}} \\ \text{Sym.} & \dfrac{\partial^2 \hat{r}_s^{(i)}}{\left[\partial \hat{\mathbf{p}}_{m,s}\right]^2} \end{bmatrix} \begin{bmatrix} \delta \hat{\mathbf{p}}^{(i)} \\ \delta \hat{\mathbf{p}}_{m,s} \end{bmatrix} \\ &= \frac{1}{2}\begin{bmatrix} \left[\delta \hat{\mathbf{p}}^{(i)}\right]^T & \left[\delta \hat{\mathbf{p}}_{m,s}\right]^T \end{bmatrix} \begin{bmatrix} \boldsymbol{\Psi}_s^{(i)} & -\boldsymbol{\Psi}_s^{(i)} \\ \text{Sym.} & \boldsymbol{\Psi}_s^{(i)} \end{bmatrix} \begin{bmatrix} \delta \hat{\mathbf{p}}^{(i)} \\ \delta \hat{\mathbf{p}}_{m,s} \end{bmatrix} \end{aligned} \quad (6)$$

Computation of the second order gradient terms is greatly simplified by noting that for each range measurement, the Hessian matrix is composed of identical sub-blocks. In 2-dimensions, each of these sub-blocks is given by

$$\boldsymbol{\Psi}_s^{(i)} = \frac{1}{\left[\hat{r}_s^{(i)}\right]^3} \begin{bmatrix} \left(\Delta y_s^{(i)}\right)^2 & -\Delta x_s^{(i)} \Delta y_s^{(i)} \\ \text{Sym.} & \left(\Delta x_s^{(i)}\right)^2 \end{bmatrix} \quad (7)$$

A similar expression applies for 3-dimensional geometries.

The range equations for a single sample point s along the trajectory are easily combinable into a single equation involving the vectors of range measurements $\delta \mathbf{r}_{s,k}$ and the system states $\delta \mathbf{z}_{s,k}$ at the iteration step k.

$$\delta \mathbf{r}_{s,k} = \mathbf{G}_{s,k} \cdot \delta \mathbf{z}_{s,k} + \mathbf{Z}\left(\delta \mathbf{z}_{s,k}\right) \cdot \mathbf{H}_{s,k} \cdot \delta \mathbf{z}_{s,k} \quad (8)$$

$$\mathbf{Z}\left(\delta \mathbf{z}_{s,k}\right) \equiv \begin{bmatrix} \left[\delta \mathbf{p}^{(1)}\right]^T & \left[\delta \mathbf{p}_{m,s}\right]^T & \cdots & \mathbf{0}_{1,D} & \mathbf{0}_{1,D} \\ \vdots & \vdots & \ddots & \vdots & \vdots \\ \mathbf{0}_{1,D} & \mathbf{0}_{1,D} & \cdots & \left[\delta \mathbf{p}^{(N)}\right]^T & \left[\delta \mathbf{p}_{m,s}\right]^T \end{bmatrix} \quad (9)$$

$$\mathbf{H}_{s,k} \equiv \begin{bmatrix} \mathbf{0}_{D(N+1),N} & \begin{matrix} \boldsymbol{\Psi}_s^{(1)} & \cdots & \mathbf{0}_D & -\boldsymbol{\Psi}_s^{(1)} \\ -\boldsymbol{\Psi}_s^{(1)} & \cdots & \mathbf{0}_D & \boldsymbol{\Psi}_s^{(1)} \\ \vdots & \ddots & \vdots & \vdots \\ \mathbf{0}_D & \cdots & \boldsymbol{\Psi}_s^{(N)} & -\boldsymbol{\Psi}_s^{(N)} \\ \mathbf{0}_D & \cdots & -\boldsymbol{\Psi}_s^{(N)} & \boldsymbol{\Psi}_s^{(N)} \end{matrix} \end{bmatrix} \quad (10)$$

In these relations N is the number of stationary transceivers composing the array, and D is the dimension (2-D or 3-D) of the array.

The equations for each of the sample points may then be combined into a single global equation describing the entire array, including all of the points along the trajectory. The outward form of the resultant relation is the same as Equation 8, although it naturally contains many more terms.

$$\delta \mathbf{r}_k = \mathbf{G}_k^* \cdot \delta \mathbf{z}_k + \mathbf{Z}\left(\delta \mathbf{z}_k\right) \cdot \mathbf{H}_k^* \cdot \delta \mathbf{z}_k \quad (11)$$

At this point it is necessary to impose coordinate constraints on the global set of equations, because an SCPA only provides relative positioning within the array and does not locate the array with respect to inertial space. These constraints may be applied through Lagrange multipliers, or by simply specifying a coordinate system. For this discussion it is simplest to specify that stationary transceiver #1 is located at the origin and stationary transceiver #2 is along the x-axis.

This eliminates several columns in $\mathbf{G}_k^*$ and $\mathbf{H}_k^*$, causing both to become full rank.

Solving Equation 11 is still difficult because of the presence of the system states in the block diagonal matrix $\mathbf{Z}(\delta\mathbf{z}_k)$. Because it involves perturbations around a nominal state estimate, however, it is possible to solve it in an iterative manner using a 2-step cascaded solution method. Although the quadratic term is not represented exactly, it still exerts a strong influence on the local gradient and greatly improves the performance of the algorithm in situations with large initial estimate errors.

The first stage of the solution process is to solve the linearized system of equations as in the basic ILS algorithm. Taking the left pseudo-inverse of the first half of Equation 11 gives

$$\delta\mathbf{z}'_k = \left(\mathbf{G}_k^{*\,\mathrm{T}} \cdot \mathbf{G}_k^*\right)^{-1} \mathbf{G}_k^* \cdot \delta\mathbf{r}_k \qquad (12)$$

The resulting state perturbation estimate $\delta\mathbf{z}'_k$ is used to construct the matrix $\mathbf{Z}'(\delta\mathbf{z}'_k)$, which is then substituted into Equation 11. This results in a new linear equation of the form

$$\begin{aligned}\delta\mathbf{r}_k &= \left(\mathbf{G}_k^* + \mathbf{Z}'(\delta\mathbf{z}'_k)\cdot\mathbf{H}_k^*\right)\cdot\delta\mathbf{z}_k \\ &= \mathbf{J}_k \cdot \delta\mathbf{z}_k\end{aligned} \qquad (13)$$

which is then solvable by taking the left pseudo inverse of the resultant linear matrix.

The QILS algorithm iteration progression is summarized in Figure 4.

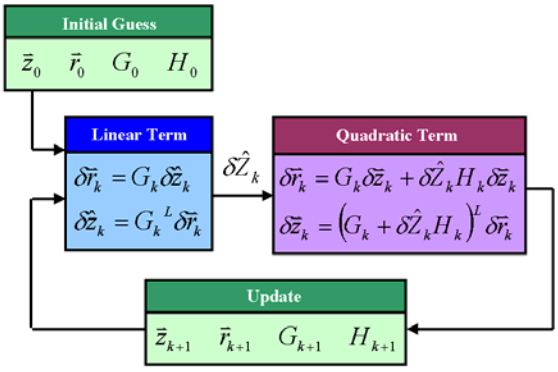

Figure 4: QILS Algorithm

5.4 Multiply-Seeded Algorithm

Significant improvement to both the ILS and QILS success rates may be made through careful examination of the modes in which it fails. Except near singularities the general failure mode is convergence to false local minima, as opposed to a general failure to converge at all. In addition, correct convergence can sometimes be highly sensitive to both the actual transceiver locations and the initial position estimate.

It is possible to overcome these difficulties through the use of multiple seedings of the basic solution algorithms. The initial positions are computed using code-based ranging as before, and then the ILS or QILS algorithms are run multiple times on the batch ranging data as usual. Before each run, however, the estimated locations of the stationary transceivers are shifted by random distances of roughly 10-20% of the array size. This change in the seed values for the ILS/QILS algorithms causes some of the solutions to fall into local minima, while others will converge to the correct global minimum. A comparison of the RMS residuals ($\delta r^T \delta r$) is usually able to quickly eliminate the erroneous solutions.

5.5 Algorithm Comparison

Because of the non-linear nature of the SCPA there is no known closed-form solution for evaluating the effectiveness of the self-calibration solution algorithms. Extensive Monte-Carlo simulations are therefore the most effective method for determining self-calibration effectiveness under the wide range of possible array configurations.

Figure 5 presents the standard configuration used for these simulations. Three stationary transceivers – the minimum number – are arrayed in a triangle. One is at the origin and the second along the x-axis. The final stationary transceiver is nominally located at the point (0.5,1.0), although it may be moved in order to change the array shape.

A fourth transceiver is located on a mobile platform and moves in a looping trajectory such as the one shown. The radius of the curves – and hence the proximity of the rover to the static transceivers – may be varied as well. Range measurements are taken at periodic sample points. The range measurements between the transceivers contain biases of common magnitude but random direction. Using the same magnitude range bias for each transceiver pair is physically unrealistic because the equivalent code-based errors would be mostly random, but it does allow for easy evaluation of the algorithms with respect to the bias size. The biases also affect the ranges between the

stationary transceivers themselves, and therefore warp the initial estimate of the array configuration.

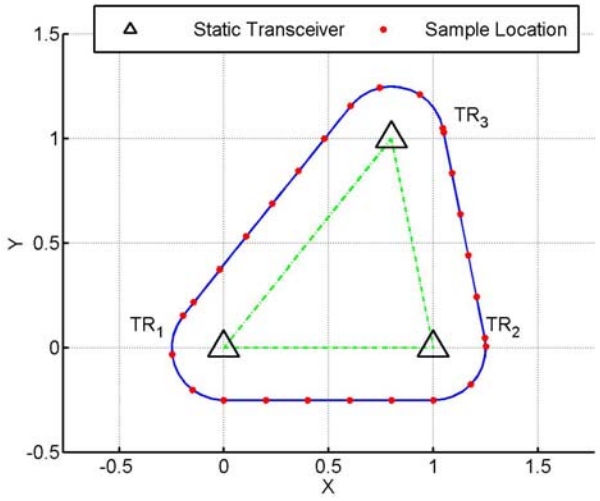

Figure 5: Standard Array Configuration

Linear Algorithm

Figure 6 shows results from simulating the baseline ILS self-calibration algorithm. Transceiver #3 is located at its nominal position to form a near-equilateral triangle, while the bias magnitude and the trajectory curve radius is varied. As long as the mobile transceiver maintains a reasonable separation from the array itself, the ILS algorithm converges to the correct array configuration 100% of the time for biases less than or equal to 10% of the array size, and with approximately 80% success for biases equal to 20% of the array size. With greater biases, convergence drops off rapidly.

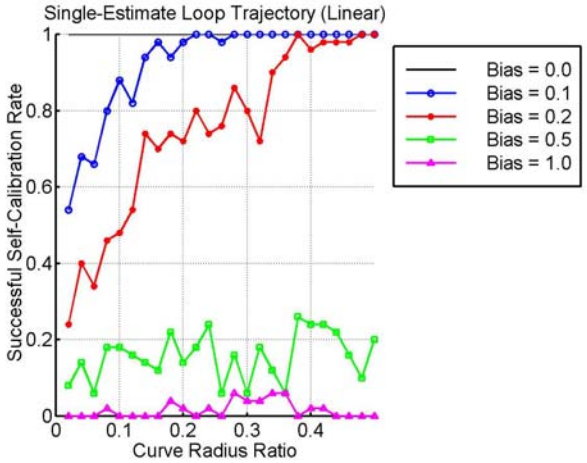

Figure 6: ILS Success vs. Curve Radius

Such convergence properties may be acceptable with larger arrays in low-multipath environments: for an array 100 meters across the initial multipath errors or other biases could be as great as 10 meters and not adversely affect the self-calibration. Smaller arrays or more severe multipath environments could lead to unsuccessful self-calibration, however, so it is important to have more effective algorithms for array self-calibration.

Quadratic Algorithm

Figure 7 presents results from the same set of simulations as were applied to the linear ILS algorithm, but now applied to the QILS algorithm. For smaller biases (up to 20% of the array size) there is only limited improvement, because in this situation the linearization is reasonably accurate. With larger biases, however, the QILS algorithm shows marked improvement, raising the success rate for a 50% bias from under 20% to approximately 70%. Even biases as large as the array itself are now removable, although at a low success rate.

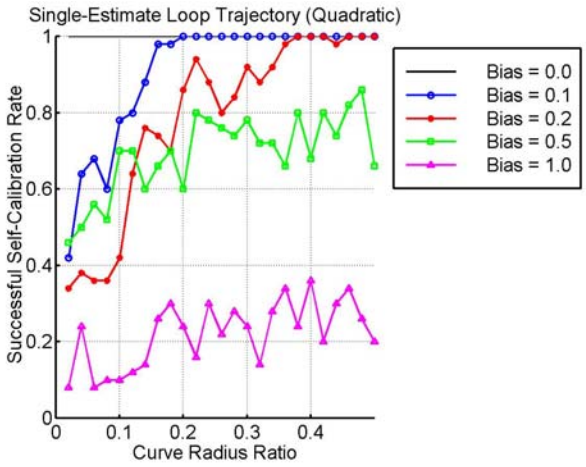

Figure 7: QILS Success vs. Curve Radius

The improvement that the QILS algorithm provides in situations with large biases is evident when one examines the relative magnitudes of the linear and quadratic components of the solution. Figure 8 presents the ratio of the matrix norms of $\mathbf{G}_k^*$ and $\mathbf{Z}'(\delta\mathbf{z}'_k)\cdot\mathbf{H}_k^*$ from a set of Monte-Carlo simulations similar to those yielding Figure 7. It is apparent that when the biases become equal to 30% of the array size, the quadratic term – which is completely ignored in the standard linear formulation – becomes as large as the linear term, and for larger biases it completely dominates the solution. (For very large biases the maximum influence of the quadratic term is actually under-represented in this plot because the cascaded solution method forces solution of the linear problem first. If the linear method completely diverges then the quadratic term can no longer be calculated and the ratio of the matrix norms is undefined.)

Table 1: Algorithm Success Rates

	Maximum Bias Value		
Algorithm	**0.2**	**0.5**	**1**
Linear ILS, Single	0.9085	0.5300	0.1359
QILS, Single	0.9130	0.7208	0.5791
Linear ILS, Multiple	0.9998	0.9582	0.6502
QILS, Multiple	1.0000	0.9978	0.9980

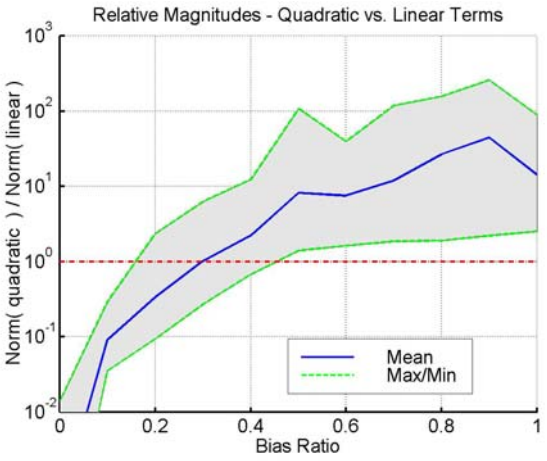

Figure 8: Linear/Quadratic ILS Comparison

Multiple-Estimate Algorithms

Figure 9 shows the QILS success rate with respect to loop radius for the same Monte-Carlo simulation performed earlier. Twenty different starting points for the algorithm were employed. In this case successful convergence to the correct solution is achieved nearly 100% of the time, except when the rover passes very near the singularities associated with the positions of the stationary transceivers. A portion of the other failures may be due to artificial numerical singularities caused by the discrete-valued simulation parameters. This plot shows how the multiple-seeding process reduces the sensitivity of the self-calibration algorithms to certain parameters such as the shape of the rover trajectory.

Array Geometry Comparison

Although the sizes of the initial estimation biases are a very strong factor in self-calibration success, these simulations have shown that the actual trajectory followed by the mobile transceiver is only a minor contributor. A much more important consideration is the shape of the array itself. While the nominal configuration is a nearly equilateral triangle, practical considerations arising from the likely autonomous deployment of the system and the potential for rugged terrain make the actual triangular shape highly uncertain. It is therefore necessary to evaluate each of the algorithms for a range of geometries, which can be easily done by holding the locations of two of the transceivers fixed and varying the location of the third.

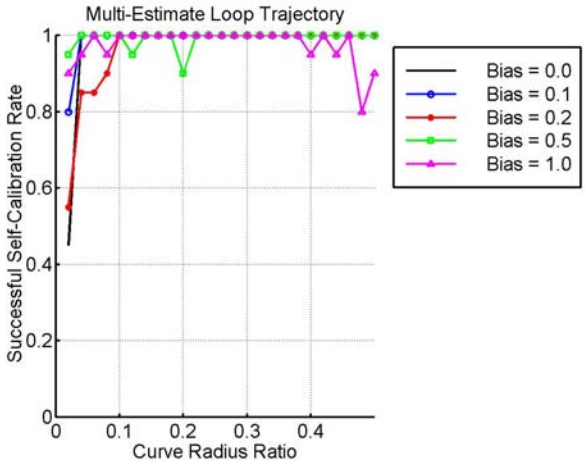

Figure 9: Multi-Estimate Success vs. Curve Radius

Table 1 presents the success rates from a set of 90,000 Monte-Carlo simulations of the array self-calibration with varying geometries. For each test, each of the four algorithms is applied to exactly the same set of configuration parameters. The size of the rover trajectory radius is uniformly varied from 0.05 to 1 units, and the biases are uniformly varied from zero up to the maximum values listed in the table. The multiply-seeded algorithms are allowed a maximum of 50 re-seeds.

The geometry for these simulations consists of two stationary transceivers at the locations (0,0) and (1,0), with the third stationary transceiver location varied by up to ± 1 unit around its nominal position of (0.5,1). The critical region in which success is calculated lies inside a circle of magnitude 0.75 centered at the nominal transceiver #3 location. This represents a worst-case estimate of the potential placement errors for the transceiver, assuming that the nominal location is the actual target.

The first bias of 0.2 represents the expected nominal operating performance of the SCPA if it were deployed in the Martian environment. This would correspond to up to 20 meters of multipath for a 100 meter wide array, a value at the upper bounds of what is normally observed during system testing. At this bias level the QILS algorithm offers little advantage over the linear ILS algorithm. The multiply-seeded algorithms both perform almost flawlessly, yielding successful self-calibration within the critical region of 99.98% and 100% for the linear ILS and QILS variants, respectively.

The case with maximum bias of 0.5 represents a very strong multipath case. At this level the QILS algorithm gives almost a 20% improvement over the linear

algorithm, while the multiply-seeded variants are still very close in performance.

A bias of up to 1.0 represents very strong multipath or other code-phase errors, equal in magnitude to the size of the array itself. For large arrays this is an extreme case, but for smaller arrays a very possible occurrence. At this level of initial error the multiply-seeded linear algorithm begins to fail, whereas the multiply-seeded quadratic algorithm continues to accurately determine the true array geometry with 99.80% success.

Figure 10 presents the self-calibration success rates from these simulations as a function of transceiver #3 location for all four algorithms for the situation with the maximum bias as large as the array size. The contours of equal success rate are plotted in 10% increments except for the multiply-seeded QILS algorithm, which uses contours at 100%, 98%, 95%, 90%, 50%, and 0% for clarity. It is clear from these plots that there is an extremely large region in which the multiply-seeded QILS algorithm yields 100% success.

6. Experimental System

A fully operational SCPA has been constructed in order to validate the basic system concepts and the resulting navigation and self-calibration performance. The current prototype includes four operational transceivers: three in stationary locations and one mounted on the rover. This is the minimum number of static transceivers needed for both unambiguous dynamic positioning of the rover and for the array self-calibration algorithm. System performance and robustness may be improved by adding

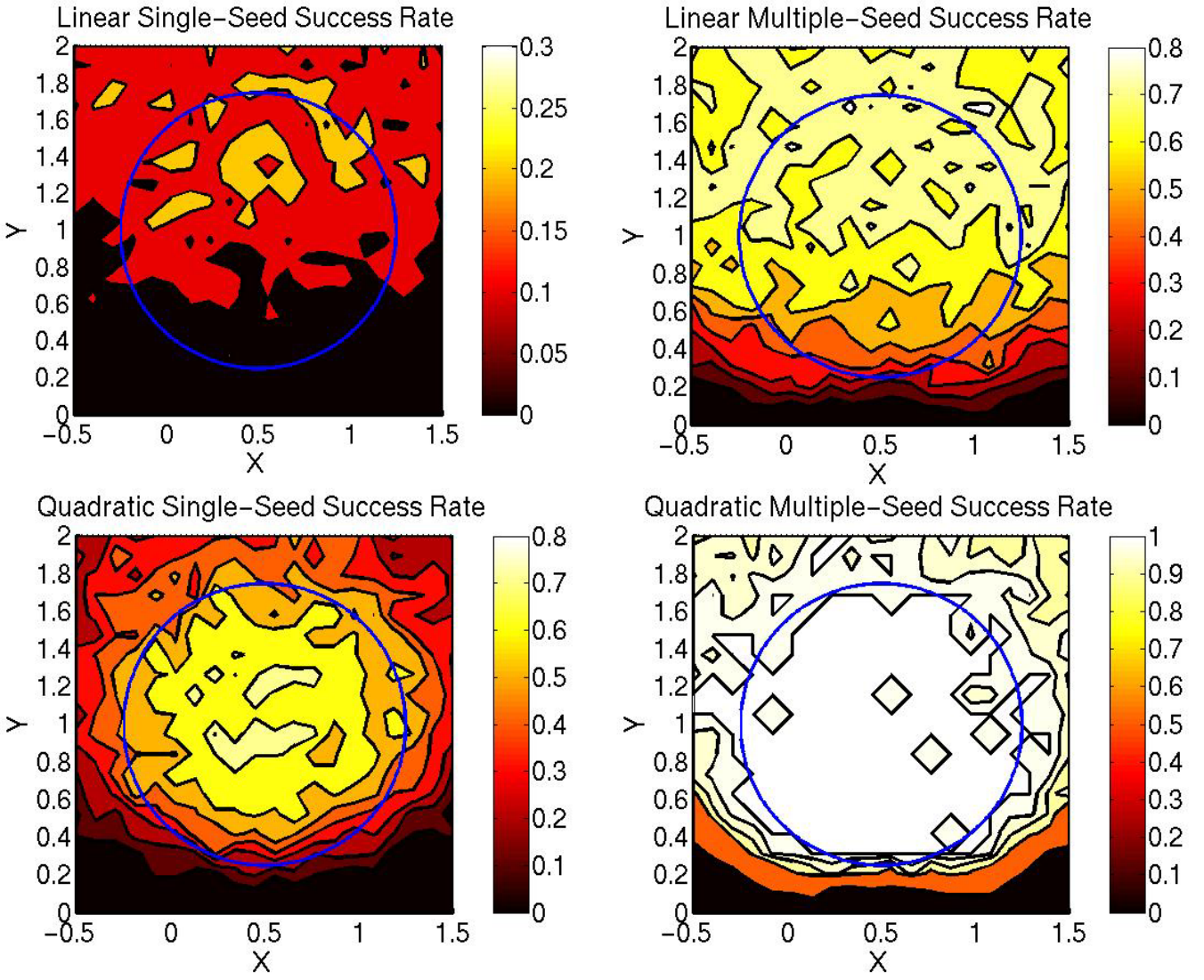

Figure 10: Algorithm Success Rates With Respect To Transceiver #3 Location (Max Bias = 1.0)

Figure 11: Static Transceiver

redundant transceivers to the array. Other system components include the ground station computer and the rover testbed.

The following is a brief summary of the hardware and software components of the SCPA. A more comprehensive description of the experimental system appears in LeMaster and Rock (2000).

6.1 GPS Transceiver Array

Each transceiver consists of a single GPS receiver and a separate pseudolite signal generator. The receiver monitors the pseudolite output signal to form a self-differencing transceiver, as described in Stone et al. (1999). The receiver is a slightly modified Mitel Orion receiver with custom tracking loops for the non-standard pseudolite data message. While the Mitel chipset is not currently space qualified, it has undergone over one year of successful on-orbit operations (Purivigraipong et al., 2000). The pseudolite is an IntegriNautics IN200C signal generator utilizing a 3% duty cycle RTCM pulsing scheme to help combat the near/far problem associated with near-field operations. The total combined broadcast power of the current experimental system is less than 1μW. (This limit is set by the FCC, which allows users with an experimental license to intentionally broadcast on L1 with a maximum continuous power of 1μW.) The low signal power limits the range of operation of the prototype system to about 30-50 meters. Higher power levels will enable operation over baselines of kilometers, provided that line-of-sight is maintained.

The transceiver is carried in a portable tote-bucket together with a 1.6 Mbps Proxim RangeLan2 wireless link for data collection and a 4.4 A-hr NiCd battery pack, which gives roughly 4 hours of continuous operation. Broadcast and reception of the pseudolite signals is accomplished through a pair of custom dipole antennas mounted on a tripod near each transceiver, as is shown in Figure 11. Using dipoles instead of commercial GPS patch antennas allows 360° operations around the transceiver because of the omnidirectional pattern and the lack of circular polarization, although this comes at the penalty of losing some multipath rejection.

The ground-station computer used for central data processing is a 133MHz Pentium laptop running a Windows NT operating system. The ground station runs a custom software program that collects the raw data from the transceiver wireless units, combines common-epoch measurements into ranges between transceiver pairs, and computes the array geometry. It also allows remote control and diagnostics of the receivers.

Figure 12: K9 Rover

6.2 K9 Rover

The rover chosen for these experiments is the NASA Ames K9 rover, shown in Figure 12. This is a variant of the FIDO rover under development at JPL for future Mars missions. It features a rocker-bogie suspension system, 360° variable steering, and an onboard dead-reckoning system. Typical speed of operation is roughly 9 cm/sec. The large sensor mast holds a stereo camera pair used for terrain mapping. A scanning laser rangefinder is mounted on the front of the rover for obstacle detection. The short vertical mast on the far left corner in the photo holds the GPS antennas used for the onboard transceiver.

In the current experimental prototype, the SCPA navigation system is not fully integrated into the K9 navigation and control system. The rover is therefore driven open loop by a human operator, with the transceiver only operating as a piggyback experiment. Future versions of this system will feature a full integration of the SCPA navigation system with the rest of the rover sensors.

7. Field Tests

7.1 Test Location

Field testing of the SCPA using the K9 rover was conducted at NASA Ames Research Center at Moffett Field, California. This was done in a large empty lot near the inlet of the large 80' by 120' subsonic wind tunnel, yielding a moderately high multipath environment. Figure 13 shows the experimental system in operation, including all three static transceivers (placed in a triangle approximately 10 meters apart) and the K9 rover. Other testing without the K9 rover has been performed on a large open field at Stanford University, a relatively low-multipath environment (LeMaster and Rock, 2000).

Figure 13: NASA Ames Test Site

7.2 Experimental Results

The goal of these tests was to validate the level of performance that could be achieved using a SCPA. The first set of results demonstrates the accuracy of the code-based and carrier phase based solutions for a static array in near ideal conditions. The second set of results demonstrates the accuracy with which a rover's position could be calculated as it moves through an array. The final set of results shows the accuracy with which the array can determine the location of the static transceivers during the self-calibration process. The results from these tests demonstrate both navigation and self-calibration with cm-level accuracy.

Test 1: Static ranging

Several tests were conducted with all of the transceivers in known, stationary locations to evaluate the stability of the static ranging measurements between the transceivers. Accuracies with the pseudolites at full duty cycle (no pulsing) are better than 1.3 meters and 0.8 cm RMS for code-based and carrier-based ranging, respectively. When the pseudolite duty cycle is reduced to 3% via pulsing, the code-based ranging accuracy degrades by approximately a factor of 3 because of the reduced SNR of the tracked signal. Carrier-based ranging accuracy remains largely unaffected.

Test 2: Dynamic ranging

Figure 14 shows a trajectory used to demonstrate the stability of the ranging measurements under dynamic conditions. Three of the transceivers were placed in known, static locations at the vertices of a 10m equilateral triangle. The fourth transceiver was started at a known location and was then carried by hand for 12 consecutive loops around the array, finally returning to its starting location. The transceiver was placed at pre-surveyed reference locations (indicated by squares) during each loop to assess the positioning accuracy.

Analysis of the data shows no significant long-term accuracy degradation even with the added dynamic stress caused by the transceiver motion. RMS positioning accuracy at the reference points was 12.4 cm, slightly worse then the technical placement error (the estimated accuracy with which the transceiver tripods can be placed with respect to the reference points) of approximately 10 cm for the mobile transceiver. When the data are corrected to account for a 39.0 cm (~2λ) carrier-phase cycle slip in one of the ranging measurements midway through the experiment, the RMS positioning accuracy improves to 4.5 cm, approximately equal to the placement accuracy of the transceivers with respect to the truth system.

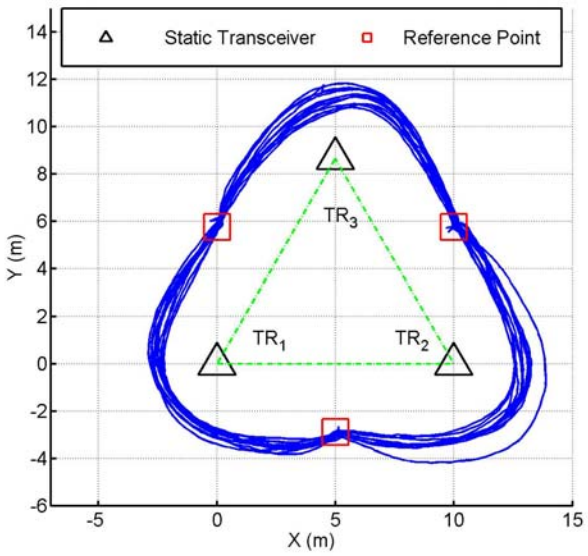

Figure 14: Mobile Transceiver Ground Track

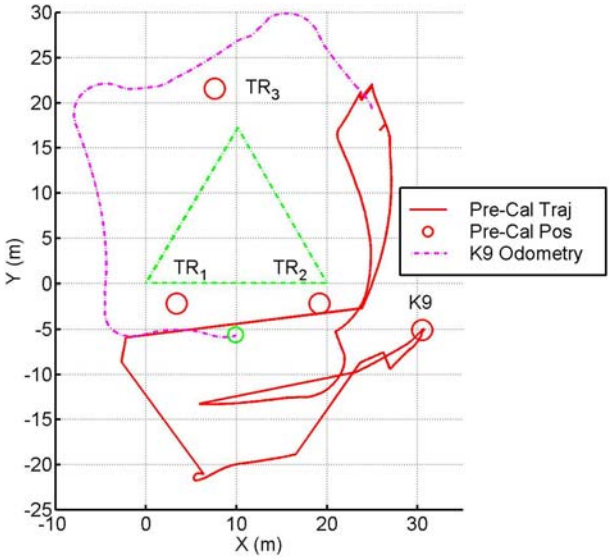

Figure 15: Pre-Calibration Positions and Trajectory

Test 3: Array self-calibration

The final set of experiments was conducted at NASA Ames in May of 2001, and follows the self-calibration process described in Section 3.2. The stationary transceivers are arrayed in the test area in a triangular configuration 20 meters to a side. The rover starts outside of the array near one edge of the triangle. The locations of these transceivers are pre-surveyed to provide a truth metric; knowledge of these positions, however, is not used at any time during the self-calibration process. Once the array is in place, averaged code-range measurements between the transceivers are used to generate an initial estimate of the transceiver locations. Figure 15 shows the transceiver locations as determined by this coarse calibration step. The actual locations are at the corners of the large dotted triangle, while the true rover position is at the small circle underneath the triangle.

Table 2 shows the corresponding position errors. The errors for the stationary transceivers are 2.76 meters RMS, an acceptable result for code-phase positioning. The positioning error for K9 is greater than 20 meters, however, most likely due to strong multipath from the surrounding fence. With such a small array, errors of this magnitude greatly cripple its navigational effectiveness.

The K9 rover now circumnavigates the array via teleoperation to provide the geometry change needed for self-calibration. The overall trajectory is approximately 100 meters in length, and takes 20 minutes to complete. During the trajectory carrier-range data is collected between the transceiver on K9 and each of the stationary transceivers, the carrier phase integers having been estimated from the results of the code-phase calibration. Figure 15 presents the rover trajectory as determined from these carrier-phase range measurements. Rather than a smooth loop around the array, the large errors in the integer estimates have produced an almost unrecognizable hash of segments and jumps. For comparison the path computed by the wheel encoders onboard K9 is also presented as a dashed line. Although the odometry trajectory does not return to the starting point like the true trajectory, the character of the loop is readily apparent.

Table 2: Initial (Code-Phase) Position Errors

Transceiver	X (m)	Y (m)
1	3.38	-2.13
2	-0.87	-2.13
3	-2.52	4.27
K9	20.42	0.60

The self-calibration algorithm is now applied to the range data collected during the preceding trajectory. Even with such large initial errors in the array estimate, the algorithm successfully converges to the correct array geometry and rover path. Figure 16 shows these results, and the corresponding errors in the locations of the stationary transceivers are displayed in Table 3. The calculated trajectory now matches the true trajectory to within centimeters, and RMS position errors for the stationary transceivers have been reduced to 4.2 cm RMS. The error associated with K9 is slightly higher because a hardware failure in one of the receivers during testing caused a loss of clock synchronization, creating a slight drift in the measured ranges.

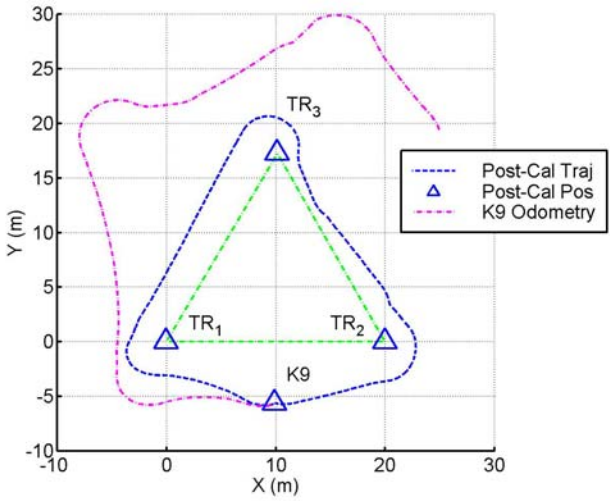

Figure 16: Post-Calibration Positions and Trajectory

8. Conclusions

The Self-Calibrating Pseudolite Array described herein provides an effective means of acquiring CDGPS-type precise positioning in locations without access to the terrestrial GPS constellation, such as on the surface of Mars. Knowledge of the locations of the (autonomously deployed) pseudolites is necessary for successful navigation within the array. Using the special algorithms together with limited motion of one of the GPS transceivers, the positions of the array elements may be determined to centimeter-level accuracy.

The self-calibration algorithms described in this paper yield successful localization of the array elements even in the presence of large relative code-phase errors such as occur with small arrays or in high-multipath environments. The QILS algorithm, by including the more dominant second-order effects, increases the calibration success rate over standard linear ILS by a factor of 2-3 times for intermediate-sized biases (i.e. up to 50% of the array size). Multiply-seeding the QILS algorithm yields 100% self-calibration success under normal operating conditions, and 99.80% success under worst-case conditions. This reliability makes it practical to implement an SCPA as a critical component in an integrated Mars-based navigation system.

Table 3: Final (Carrier-Phase) Position Errors

Transceiver	X (m)	Y (m)
1	-0.01	0.03
2	-0.05	0.03
3	0.06	-0.05
K9	-0.16	0.09

The field tests conducted at NASA Ames Research Center using the K9 Mars rover prototype demonstrate the viability and accuracy of the SCPA. Code-level positioning errors in low-multipath situations are less than 3 meters, sufficient for coarse-level navigation over wide areas. Once carrier-phase self-calibration has been conducted, positioning accuracy increases to better than 5 cm RMS, a level which would enable precise control and cooperative operations between multiple robots.

Although the Self-Calibrating Pseudolite Array described in this paper is capable of providing extremely accurate and repeatable navigation without any additional augmentation, an SCPA on the Martian surface would ideally be used in conjunction with a complementary set of sensors in order to provide additional information beyond the scope of the raw GPS-based position data. Computer vision or scanning lasers, for example, would be required for obstacle detection and avoidance, and would also be useful for fine servoing control. Additionally, blending the SCPA navigation data with an inertial navigation or dead reckoning system would provide an additional level of robustness in case of GPS cycle slips or signal loss due to intervening terrain or other obstacles. Because of its capability for centimeter-level, drift-free positioning for multiple agents, an SCPA would be a critical enabling technology for such an integrated sensing and navigation system.

Acknowledgements

This research has been conducted under NASA grants NCC2-1154 and NAG2-1464 as part of a joint effort between Stanford University Aerospace Robotics Laboratory and the NASA Ames Research Center. We would especially like to thank Maria Bualat, Mike Fair, and Anne Wright at ARC for their efforts in making these joint field tests possible.

References

Bresina, John L., et al., "K9 Operation in May '00 Dual-Rover Field Experiment", 6th International Symposium on Artificial Intelligence and Robotics & Automation in Space, St-Hubert, Quebec, Canada, June 2001.

Chung, Hakyoung, et al., "Accurate Mobile Robot Dead-Reckoning with a Precision-Calibrated Fiber-Optic Gyroscope", IEEE Transactions on Robotics and Automation, Vol. 17, No. 1, February 2001.

Ely, Todd A., et al., "Mars Network Constellation Design Drivers and Strategies", AAS/AIAA Astrodynamics

Specialist Conference, Girwood, Alaska, Aug. 1999. (AAS 99-301)

Guivant, Jose, et al., "Simultaneous Localization and Map Building Using Natural Features in Outdoor Environments", Intelligent Autonomous Systems 6, Vol. 1, IOS Press, Berlin, Germany, July 2000, pp. 581-588.

Huntsberger, Terry, et al., "Rover Autonomy for Long Range Navigation and Science Data Acquisition on Planetary Surfaces", IEEE International Conference on Robotics and Automation, Washington, DC, May 2002.

LeMaster, E.A., Rock, S.M, "Self-Calibration of Pseudolite Arrays Using Self-Differencing Receivers", Proceedings of the Institute of Navigation GPS-99 Conference, Nashville, TN, Sept. 1999, pp. 1549-1558.

LeMaster, E.A., Rock, S.M, "Field Test Results for a Self-Calibrating Pseudolite Array", Proceedings of the Institute of Navigation GPS-2000 Conference, Salt Lake City, UT, Sept. 2000, pp. 1046-1055.

Neilan, Ruth E., et al., "International GPS Service 2000: Life without SA", Proceedings of the Institute of Navigation GPS-2000 Conference, Salt Lake City, UT, Sept. 2000, pp. 438-446.

Olson, Clark F., et al., "Stereo Ego-motion Improvements for Robust Rover Navigation", IEEE International Conference on Robotics and Automation, Seoul, South Korea, May 2001.

Parkinson, B. et al., ed., Global Positioning System: Theory and Applications, Vols. I & II, American Institute of Aeronautics and Astronautics, 1996.

Purivigraipong, S., et al., "Demonstrating GPS Attitude Determination from UoSat-12 Flight Data," Proceedings of the Institute of Navigation GPS-2000 Conference, Salt Lake City, UT, Sept. 2000, pp. 2625-2633.

Schenker, P. S., et al., "FIDO: a Field Integrated Design & Operations Rover for Mars Surface Exploration", 6th International Symposium on Artificial Intelligence and Robotics & Automation in Space, St-Hubert, Quebec, Canada, June 2001.

Stone, J., et al., "GPS Pseudolite Transceivers and their Applications", Proceedings of the 1999 Institute of Navigation National Technical Meeting, San Diego, CA, Jan. 1999.

Willams, Stefan B., et al., "Autonomous Underwater Simujltaneous Localization and Map Building", Proceedings of the IEEE International Conference on Robotics and Automation, San Fransisco, CA, April 2000.